Freie Universität Berlin

Title:

Imaging of Bandtail States in Silicon Heterojunction Solar Cells: Nanoscopic Current Effects on Photovoltaics

Author(s):

Mandefro Y. Teferi, Hans Malissa, Anna Belen Morales-Vilches, Cham T. Trinh, Lars Korte, Bernd Stannowski, Clayton C. Williams, Christoph Boehme, and Klaus Lips

Document type: Preprint

Citation:

Imaging of Bandtail States in Silicon Heterojunction Solar Cells: Nanoscopic Current Effects on Photovoltaics

Mandefro Y. Teferi,[†] Hans Malissa,[†] Anna Belen Morales-Vilches,[‡] Cham T. Trinh,[¶] Lars Korte,[¶]

Bernd Stannowski,[‡] Clayton C. Williams,[†] Christoph Boehme,[*,†] and Klaus Lips[**,§,∥]

[†] Department of Physics and Astronomy, University of Utah, 115 S 1400 E, Salt Lake City, UT

84112-0830, USA

[‡] PVcomB, Helmholtz-Zentrum Berlin für Materialien und Energie (HZB), Schwarzschildstr. 3,

12489 Berlin, Germany

[¶] Institute for Silicon Photovoltaics, Helmholtz Zentrum Berlin für Materialien und Energie

GmbH (HZB), Kekulesstr. 5, 12489 Berlin, Germany

[§] Department Spins in Energy Conversion and Quantum Information Science (ASPIN),

Helmholtz-Zentrum Berlin für Materialen und Energie GmbH (HZB), Hahn-Meitner-Platz 1,

14109 Berlin, Germany

[∥] Department of Physics, Freie Universität Berlin, Arnimallee 14, 14195 Berlin, Germany

KEYWORDS

Silicon heterojunction solar cell, conduction atomic force microscope, bandtail states, percolation, random telegraph noise, nanoscopic current paths

ABSTRACT

Silicon heterojunction (SHJ) solar cells represent a promising technological approach towards higher photovoltaics efficiencies and lower fabrication cost. While the device physics of SHJ solar cells have been studied extensively in the past, the ways in which nanoscopic electronic processes such as charge-carrier generation, recombination, trapping, and percolation affect SHJ device properties macroscopically have yet to be fully understood. We report the study of atomic scale current percolation at state-of-the-art a-Si:H/c-Si heterojunction solar cells at room temperature, revealing the profound complexity of electronic SHJ interface processes. Using conduction atomic force microscopy (cAFM), it is shown that the macroscopic current-voltage characteristics of SHJ solar cells is governed by the average of local nanometer-sized percolation pathways associated with bandtail states of the doped a-Si:H selective contact leading to above bandgap local photovoltages (V_{OC}^{loc}) as high as 1.2 V ($eV_{OC}^{loc} > E_{\text{gap}}^{\text{Si}}$). This is not in violation of photovoltaic device physics but a consequence of the nature of nanometer-scale charge percolation pathways which originate from trap-assisted tunneling causing dark leakage current. We show that the broad distribution of nanoscopic local photovoltage is a direct consequence of randomly trapped charges at a-Si:H dangling bond defects which lead to strong local potential fluctuations and induce random telegraph noise of the dark current.

INTRODUCTION

The theoretical limit of the conversion efficiency of single junction solar cells is well understood and described by the Shockley-Queisser limit (SQL).[1-3] A consequence of the SQL is that the open circuit voltage (V_{OC}) of single junction solar cells is always smaller than the bandgap energy ($eV_{OC} < E_{gap}$) and is determined by the quasi Fermi splitting $\Delta = E_{fn} - E_{fp}$ that can be achieved at the collecting contacts. Δ is limited by Auger and radiative recombination and well understood in terms of thermodynamics and determined by the quasi Fermi level distribution in the device.[4-10] There have been a few observations of V_{OC} being higher than the bandgap energy in various material systems but it seems that these effects could be explained by series connection of several intrinsic junctions. On the other hand, potential fluctuations that may develop at the selective contacts and in the bulk through charge trapping at bandtail states generated through local disorder is known to largely modulate the potential landscape of solar cells and generally lead to a decrease of V_{OC}.[11] However, on nanoscopic scales it is possible that local enhancements of the photovoltage (V_{OC}^{loc}) can happen that appear as above bandgap V_{OC}. Such effects will not be observable with conventional contacts since they would average laterally over the local fluctuations of V_{OC}^{loc}. In this report we will show that with nanometer conductive probes as provided by conduction AFM (cAFM) we are able to resolve such nanoscopic effects in conventional crystalline silicon (c-Si) heterojunction (SHJ) solar cells with hydrogenated amorphous silicon (a-Si:H) as selective contact layers.[12-14] Different from previous cAFM on silicon we probe the nanoscopic dark- and photocurrents that flow vertically through the selective contact.[15,16] With this technique, we are able to detect local I-V curves with V_{OC}^{loc} at RT which are as large as 1.2 V. We show that such large V_{OC}^{loc} are in accordance with thermodynamics and are the result of charge transfer and injection through a-Si:H bandtail- and defect-states at the charge selective SHJ interface which

leads to stochastic charge trapping and hence to fluctuations of the nanoscopic device performance which is observed as random telegraph noise (RTN) with up to 100% modulation.[17-21] This is orders of magnitude larger than what has been reported before for doped a-Si:H.[22-25] From the analysis of the cAFM images we can reconstruct a density of states which suggests that we image bandtail states in a-Si:H with a minimum localization of about 1 nm. We suggest that these states are induced by density fluctuations in the amorphous network that have recently been reported about.[26]

Tunneling through bandtail states at the a-Si/c-Si interface thus limits the performance of SHJ solar cells, and an improved understanding of these nanoscale transport processes and their relation to recombination within the SHJ is crucial for further efficiency improvements, particularly for the critical tunneling junction in tandem perovskite/c-Si solar cells.[27]
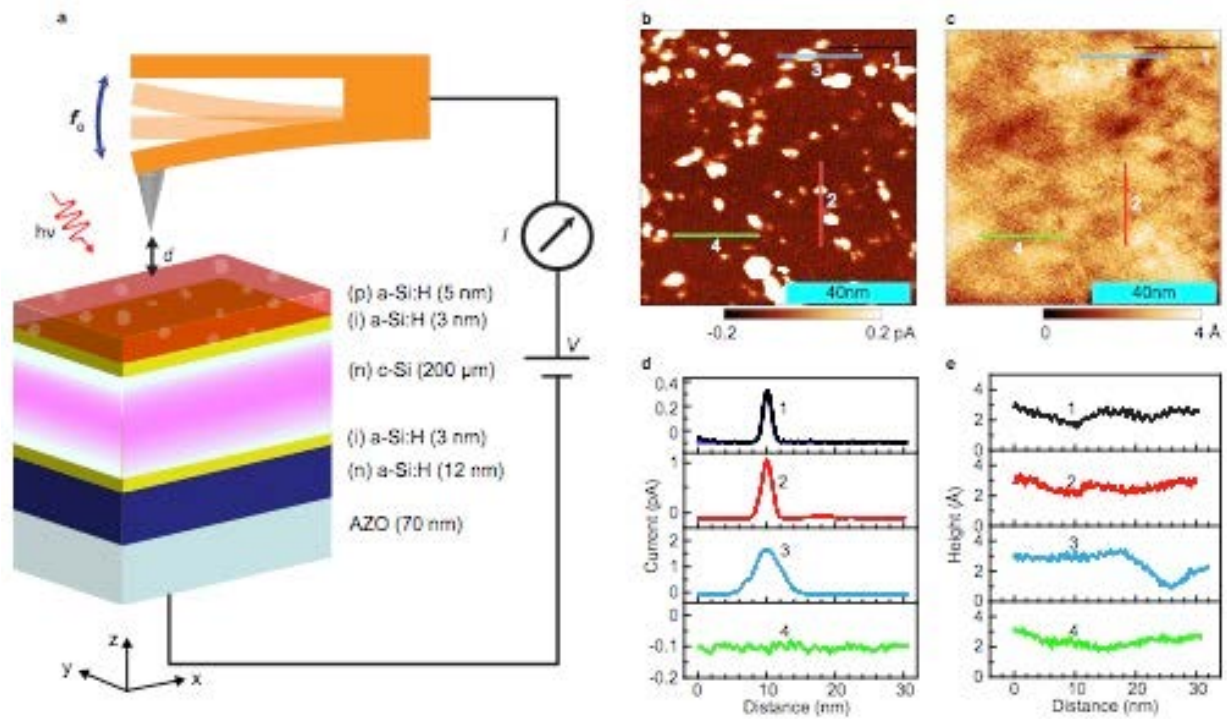
Figure 1. (a) Sketch of the RT UHV cAFM experiment on SHJ solar cell structures allowing for dark and photoconductivity measurements at various surface locations with atomic scale resolution using a scanning probe, while AFM force feedback allows for control of TSD. White light illumination was achieved with a tungsten halogen lamp. (b) Current under illumination and (c) topographic image of a 100 nm × 100 nm scan area measured using cAFM under illumination and forward bias condition on the SHJ shown in panel (a). The topographic and current images are obtained simultaneously. (d) Plots of different current profiles along the line cuts 1-4 shown in panel b. (e) The plot of the topographic height profile along the line cuts 1-4 shown in panel c. The blue curve in panel d is the fit to the data with a gaussian profile of FWHM 1 nm.

RESULTS AND DISCUSSION

Experimental Approach

We conducted a study of charge percolation across SHJs using ultra-high vacuum (UHV) conduction atomic force microscopy (cAFM) where the a-Si:H surface of the SHJ solar cell was scanned by a platinum AFM tip. For cAFM, tip-sample interaction force is used to gain topographic surface information and use this as feedback observable for the position control of the probe tip, while the tunneling current between the sample and probe tip is measured, allowing for very sensitive local surface conductivity measurements with the lower angstrom-resolution.[28-31] cAFM has been used successfully to analyze depth-dependent currents in perovskite solar cells or the role of structural defects through conductive-tomographic AFM in CdTe solar cells.[32-34] With cAFM it was also shown that at the a-Si:H/c-Si interface a 2D conductive layer exists that is responsible for some of the remarkable feature of the SHJ solar cell.[15] However, in none of those cAFM reports on solar cells current limitations due to localized states could be detected.

Figure 1a displays a sketch of a cAFM setup with a SHJ device that was processed identically to previously reported and well characterized macroscopic SHJ solar cells with device efficiencies of >20% and 23.65% (certified) on smooth and textured wafers, respectively.[35-37] The main difference of the structures used for cAFM experiments here, compared to complete solar cells, is that they did not have a transparent conducting oxide (TCO) and metal contact on the front side, since the Pt tip assumed this role on a nanometer-scale during the cAFM experiments. It should be noted that the highly conductive TCO layer (or a conventional diffused c-Si emitter contact) would lead to current spreading and therefore dramatically reduce the resolution. For the back contact, the TCO was in direct contact with the copper cAFM sample holder which also served as a good thermal bath. The cAFM setup was based on an Omicron Nanotechnology Oxford Instruments LT

STM/AFM system which is equipped with a quartz tuning fork in qPlus configuration and a commercially acquired Pt tip.[28,31,38] The tuning fork resonance frequency f_0 was ~30 kHz while a constant amplitude of ~1 nm was maintained under UHV conditions of ~10^{-10} mbar. The quartz tuning fork allows for cAFM measurements in either darkness or under well-defined illumination conditions, in contrast to optically detected AFM where the detection light can induce additional, uncontrollable photocurrent effects. Note that all experiments reported here were performed at room temperature if not stated otherwise.

Scheme 1. Schematic Illustration of the PECVD Process. The SiH_4 molecules (blue) are decomposed but mainly SiH_3 will contribute to film growth. H_2 and H radicals (red) will assist in surface teching and passivation of the a-Si:H film. PH_3 (green) and B_2H_6 (not shown) are used as dopant source gas.
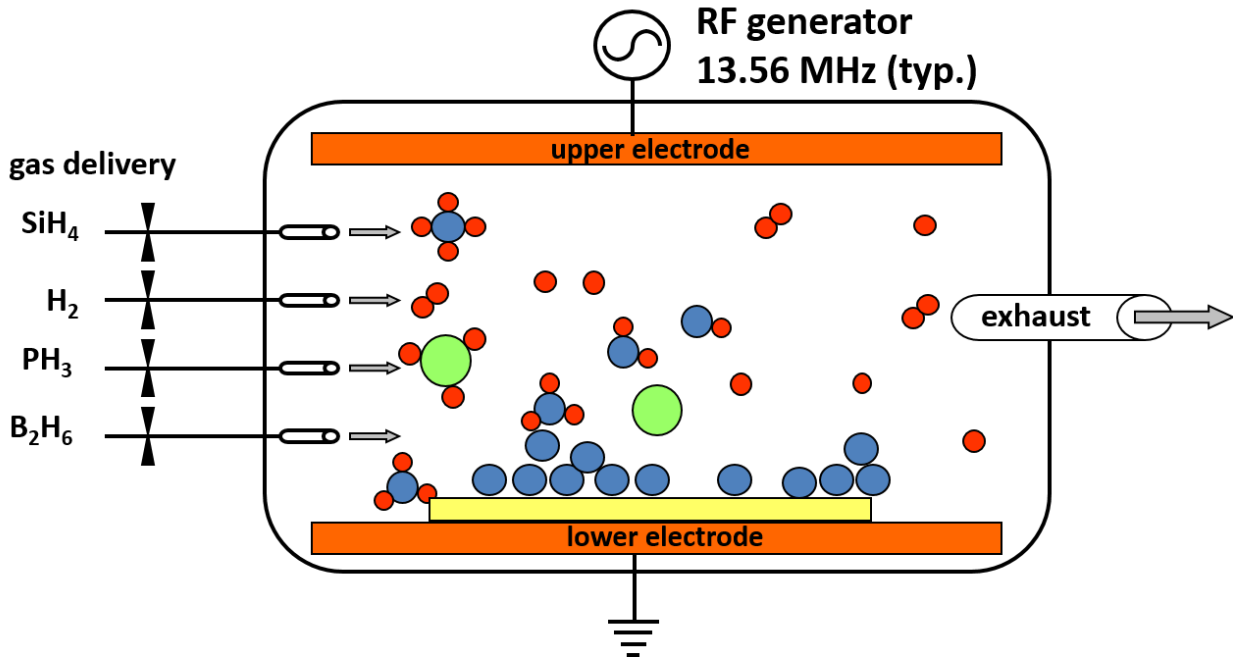
The SHJ devices studied were based on a double-sided polished n-type <100> oriented float-zone silicon wafer, with details about the sample stack and its preparation being described in the Methods section below (cf. Scheme 1). Before devices were introduced into the UHV chamber of the cAFM setup, the oxide layer and other contaminants on the uncontacted (p)-a-Si:H emitter contact layer were removed by application of a brief HF drop with 1% HF solution to the front surface of the device. The device was then mounted on the Omicron sample holder and brought into UHV conditions within 5 min after the HF dip to assure an oxide-free surface for the non-contact mode cAFM measurement. Light was applied by a heat-filtered tungsten halogen lamp with an intensity of 475 W/m^2 ($\sim$1/2 sun). Topographic images obtained from the tuning fork frequency shift, Δf, were recorded, while, simultaneously, the current between probe tip and sample was monitored such that local charge transport and topography of the SHJ can be compared. The measurement of current-voltage (I-V) characteristics required well controlled, lower angstrom-range tip-sample distances (TSD), d, in tunneling range of the sample surface, that had to be maintained at a constant value even when electrostatic forces changed, e.g. due to changing bias conditions.

Current variations on the nanometer scale

Figure 1b shows a representative current image obtained under white light illumination and a forward bias $V_{bias} = 1$ V while Figure 1c displays the simultaneously taken topographic image. The topography and the current images show different features, albeit both were recorded at the same time on the same area. While the topography shows 5 Å peak-to-peak roughness, the current under illumination (CuI) image reveals local current maxima from femtoampere to tens of picoampere with varying shapes and nanometer-range sized maxima as determined in a procedure discussed

in the Supporting Information.[39] Within these areas, referred to as current patches (CPs) in the following, the current is enhanced in magnitude compared to the current in the more homogeneous areas (HAs), where the current is much smaller in magnitude. From these images, we conclude that the current flow through the thin, boron doped a-Si:H emitter layer is highly inhomogeneous and positive with strongest deviations within the nanometer range sized CPs, while the HAs displays predominantly negative CuI. As shown in Figure 1d and 1e, line scans taken at identical positions shown in panels Figure1b and 1c, no obvious surface morphology features are observed that can be identified as the origin of the CPs. Hence, we attribute the CPs identified in Figure 1b to nanometer scale conductivity inhomogeneity of the SHJ surface- or subsurface-regions, rather than to surface morphology.

In contrast to larger CPs, the smallest CPs that we have observed can be fitted by Gaussian distributions and they typically show diameters with a full width at half maximum (FWHM) of $\sim$1 nm as shown in Figure 1d. We therefore conclude that these features in the cAFM measurements are not governed by the resolution of our setup, which is about 5 Å as determined with our cAFM for Pb centers located at the c-Si/SiO$_2$ interfaces.[40]

While the lower limit of the observed CP size is about 1 nm, the analysis of 340 different CPs recorded under identical conditions (V_{bias} = 1 V, TSD = 7 Å, cf. Supporting Information Figure S1 for more detail), we obtain a lognormal distribution of the outer CP diameter for larger CPs, peaking at $d_{CP} = (2.7 \pm 1.3)$ nm. We note that the observation of CPs at the a-Si:H/c-Si heterointerface reproduces for different V_{bias} and is not a specific feature of doping type since we observe similar CPs for SHJ cells with oppositely doped base and emitter [(n,i) a-Si:H/(p)c-Si] as shown in the Figure S2 of the Supporting Information. We therefore arrive at the conclusion that CPs are a common feature of transport through the a-Si:H/c-Si interface.

We have repeated the current mapping experiments represented by Figure 1b on various surface locations and also for different V_{bias}. Figure 2a displays such measurements made between short circuit condition ($V_{bias} = 0$ V and $V_{bias} = 1.8$ V). The resulting current maps are plotted in Figure 2a obtained with a thoroughly calibrated current detector, assuring that the varying electrostatic force conditions under varying V_{bias} did not cause changes of the absolute offset of the current detector as conceivable due to potential changes of the TSD or other influences (cf. the discussion in Supporting Information of Figure S3). The data in Figure 2a shows that, under short circuit conditions, we observe a fairly homogenous and mostly constant, albeit not entirely featureless short circuit current throughout the probed area. With increasing bias, CPs become increasingly pronounced, i.e. the current within the CPs shifts towards the forward direction, while the number of CPs increases. Some CPs appear only within narrow V_{bias} ranges and then disappear towards higher V_{bias}. Also, some CPs display a pronounced substructure with more than one local current maximum. Eventually, at larger V_{bias}, especially beyond the macroscopic V_{OC}, CPs display large positive currents whose magnitudes become exponentially larger, as expected for the forward current of a SHJ solar cell. Remarkably, this macroscopically well-known diodic I-V behavior is displayed microscopically only by the CPs, while large HAs continue to show only a negative CuI, even at $V_{bias} = 1.8$ V (cf. Figure 2c).
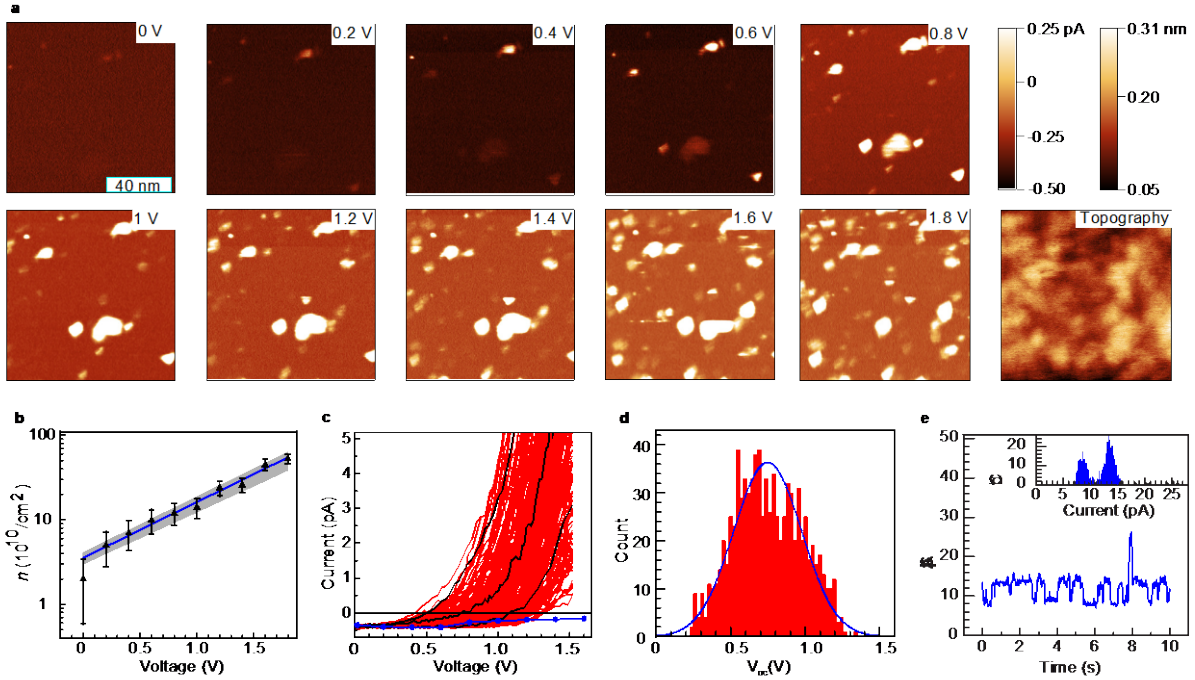
Figure 2. (a) Bias dependence of cAFM current maps of the SHJ sample shown in Figure 1a. The panels show RT cAFM current images at indicated V_{bias} measured under illumination at constant TSD. The topography was measured simultaneously and shows no significant correlation with the current maps. Current and topographic scale are shown in color code. (b) Density of CPs as function of V_{bias} extracted from panels (a) through a procedure described in the Supporting Information with error bars indicated in the figure. (c) the red curves indicate 1000 I-V curves extracted at various CPs (for details see text) I-V characteristics were obtained under ~0.5 sun illumination at various TSD between 2 Å and 7 Å in non-contact mode while the force-feedback loop was turned off. The blue dotted line represent the I-V curves obtained through integration over the HAs of the current maps in panel a. In contrast to the I-V curves recorded in CPs (red lines), diodic behavior is not apparent. (d) Histogram of the distribution of the open-circuit voltages V_{OC}^{CP} as extracted from the I-V data displayed in c. The blue curve represents a fit with a normal distribution. (e) Time evolution of the current through CP measured at $V_{bias} = 1$ V

12

exhibiting RTN. The inset shows the current distribution recorded over 10 s showing a pronounced

bimodal distribution.

Fingerprint of Urbach tail in nanoscopic PC

The topography image of the area where the cAFM data sets of Figure 2a were obtained, shows, again, no significant similarity with any of the current images. Thus, in order to investigate the physical nature of the observed CPs, we determined from the current maps the number of CPs per image, i.e. we determined the number of local current extremata by a procedure explained in the Supporting Information using *ImageJ* (see Figure S4 in the Supporting Information). The plot of the density, n_{CP} of detected CPs per area as a function of V_{bias} shown in Figure 2b reveals a good agreement with an exponential function with V_{bias} from 3×10^{10} cm^{-2} to 5×10^{11} cm^{-2}.

In order to understand the bias dependency of the CP density, we considered the shifts of the quasi Fermi levels of electrons and holes, E_{fn} and E_{fp}, respectively for $0.5 < V_{bias} < 1.8$ V. These shifts were obtained from a 2D numerical simulation *TCAD-SENTAURUS^{TM}* (see Figure S5 in the Supporting Information) of the used SHJ structure under 0.5 sun illumination (with photon absorption in the 8 nm a-Si:H layer being neglected).[41] These calculations showed that E_{fn} shifts nearly linear with V_{bias} in the p-a-Si:H region since electrons are minority carriers, while E_{fp} only shifts in the region close to the c-Si interface and is otherwise pinned due to the high doping level. Since the shift of E_{fp} will change the density of occupied bandtail states in the a-Si:H, we can determine the activation energy of the creation of CPs. We find an activation energy, $E_0 = 89 \pm 4$ meV, comparable to the Urbach energy associated with the valence bandtails in highly doped a-Si:H.[42] Thus, the increase in CP area density with V_{bias} corresponds to the change of the density of occupied states around E_{fp} in the valence bandtail of the (p)-a-Si:H layer. Essentially, this corresponds to the density of valence bandtail states that allow for hole transport, based on the assumption that these are energetically in a range of kT within E_{fp}. We therefore conclude that the observed CPs correspond to valence bandtail states or nanometer-sized regions with a certain

electronic structure where such bandtail states evolve within the (p)-a-Si:H layer. The cAFM current maps essentially represent images of such regions in the thin emitter layer of the SHJ device which have been made visible for the first time to the best of the authors knowledge.

Photovoltage variation on the nanometer level

In order to further investigate the nature of the CPs, including their statistical variance, we have measured more than 1000 I-V characteristics on various CPs in different, macroscopically well-separated surface locations under identical conditions. In order to scrutinize that the influence of the TSD and, thus, the tip to surface tunneling probability—an experimental parameter—neither affects the measured current or only in a limited and well understood way, these measurements were carried out with randomly varying TSD between 2 Å and 7 Å (see the discussion in the Supporting Information). The red plots in Figure 2c display the I-V data sets. Remarkably, for the given illumination conditions, all I-V characteristics experience about the same short-circuit current, $I_{SC} = I_{SC}^{CP} = 400$ fA, independent of the TSD. This indicates that light-induced charge generation is not altering the solar cell's photocurrent (PC) on the length scales of the experimental window (a few micrometer). As it will be shown later, at least throughout the homogeneous sample surface areas, the excess charge carriers (holes) pass through the interface into the hole selective contact without spatial selectivity, i.e. the currents at any measured point within the imaged area, does not just represent the current at the given location but instead, a current that is broadly distributed throughout the area around the probe location. Note that this primary PC as defined by McGlynn is superimposed by the dark current that is only supported through the highly localized CPs and a good proof of the superposition principle of dark and PC.[43]

While the PC appears to be homogeneous, Figure 2c also reveals that both FF and V_{OC}^{CP} vary dramatically for each CP, with V_{OC}^{CP} being even larger in some few cases than the c-Si bandgap

$(qV_{OC}^{CP} > E_{gap}^{Si})$. Figure 2d displays a histogram of the values of V_{OC}^{CP} as obtained from the I-V curves in Figure 2c, which exhibits a broad distribution that is centered at $\overline{V_{OC}^{CP}} = (748 \pm 200)$ mV, which, remarkably, is within experimental error the macroscopically expected V_{OC}^{CP} for this type of base material and surface passivation condition, as found from 2D numerical simulation (see Figure S6 in the Supporting Information). The solar cell simulation of the devices studied here assuming a Pt tip electrode, provides $V_{OC}^{sim} = 0.727$ V at @0.5 suns for a smooth surface (see Supporting Information, Figure S5) and $V_{OC}^{sim} = 0.741V$ @1sun for a solar cell with TCO and structured surface and a simulated efficiency >23%, similar to the experimental values of these cells.[35,36] Thus, the CP data (red) shown in Figure 2c suggest that a macroscopic SHJ solar cell is essentially a parallel circuit of a large number of CPs which represent microscopic SHJs.

As already seen in Figure 2a and 2c, the I-V characteristics within the HAs show nearly voltage independent CuI, with $I_{SC}^{CP} = I_{SC}^{HA}$. In Figure 2c, we have also plotted the average current obtained from HAs (blue dots connected by line). The plotted I-V behavior of HAs can be understood by the definition of HAs, which are those areas that do not show CPs within the applied bias range. This definition already implies that I-V functions within HAs will reveal no influence of the dark current injected through the CPs and result in values for V_{OC}^{HA} far beyond V_{OC}^{exp}. In essence, as long as I-V functions are measured at locations where no CPs are seen and, thus, no valence bandtail states are present, the (p,i)-a-Si:H/c-Si interface behaves like a SHJ interface with (p)-a-Si:H that allows no charge injection at low biases. Naturally, the V_{OC} of such a macroscopically non-existent interface, can be higher than V_{OC}^{exp} but cannot be larger than $V_{OC}^{Auger\ limit} = 0.75$ V for a cell thickness of 200 µm and under AM1.5 illumination.[1]

Since I_{SC}^{HA} is homogeneously distributed, and $I_{SC}^{HA} = I_{SC}^{CP}$, we attribute this lack of spatial selectivity to holes that are injected into the a-Si:H valence band from the highly delocalized two-

dimensional hole gas (2DHG) right below the (p,i)-a-Si:H/c-Si interface (see Figure 3 and its discussion below). Interestingly, these observations shown in Figure 1 and 2 imply that dark current and PC at SHJ interfaces separate in different percolation regimes: The PC is generated inside the c-Si absorber of the SHJ and the holes as minority carriers diffuse to the 2DHG at the SHJ interface. From here the excess holes percolate anywhere at that interface across the a-Si:H layers (thermally emitted or direct tunneling) through the a-Si:H valence band as shown in Figure 3a. On the other hand, the dark current (holes going from the Pt tip to the c-Si) appears to selectively percolate through the valence bandtail state. We further conclude that the dark current cannot be injected from the Pt tip into HAs. As a consequence, the HAs can be identified as those areas where we directly observe the primary PC of the SHJ device. Their I-V characteristics are similar to the PC deduced from numerical simulation (see Figure S6c in the Supporting Information). In a macroscopic device with TCO contacts this primary photocurrent cannot be measured and is always superimposed by the dark current that is established through the CPs. As shown clearly from our results, cAFM is capable of spatially separating dark and photocurrent.
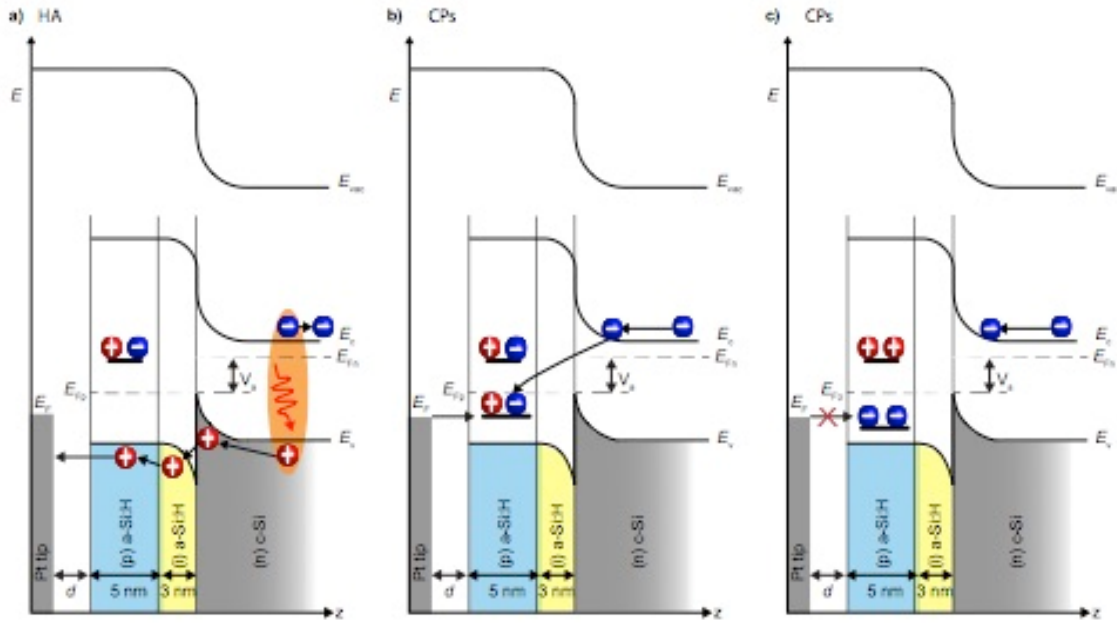
Figure 3. Illustrations of SHJ charge transfer percolation pathways of photo- and dark-currents at HAs (a) as well as CPs (b, c). Note that interface band diagrams are usually single electron state illustration and, thus, charge carriers such as electrons in the conduction bands (blue, -) and holes in the valance bands (red, +) are illustrations of individual occupied and unoccupied electron states, respectively. In contrast, in order to avoid ambiguity, the charge states of localized electronic bandgap states such as tail and dangling bond states are represented here in a two-electron picture where (+-), (++), and (--) represent neutral, singly positive as well as singly negative charge states, respectively. The images present a near open-circuit situation where the quasi Fermi-level splitting $\Delta E_f = E_{fn} - E_{fp} = V_a \sim V_{OC}$. (a) Charge extraction of photogenerated holes in HAs through tunneling of electrons in the Pt tip (below the Pt Fermi level) into the valence band of a-Si:H. (b) Injection of holes from the Pt tip in to the SHJ through electron tunneling of electrons out of the a-Si:H valence band-tail state into unoccupied electron states above the Pt Fermi level. This process represents dark current at CPs. (c) Hole injection blockade at a CP due to the presence of positive charge that is trapped at a nearby db defect state deep within the a-Si:H band gap. The

trapped charge causes the band-tail state energy level to shift closer to the valence band such that it becomes negatively charged. This leads to a complete blockade of current injection, and hence, to a significant dark current change at the CP. The dark current will fluctuate and generate RTN, when the db state is randomly charged and discharged repeatedly. The quasi-Fermi levels E_{fn} and E_{fp} are indicated by dashed lines and represent the thermodynamic situation of the band diagram, black arrows indicate transitions of electrons or holes, respectively.

The observation of a large distribution of V_{OC}^{CP} is unexpected as qV_{OC} equal to or above the band gap of the absorber is not possible from a macroscopic thermodynamics point of view, taking the band structures, Fermi-energies, and band offsets into consideration. We can exclude that the strong variation of V_{OC}^{CP} is dominated by a TSD artifact, e.g. by the tunneling gap between tip and sample causing a voltage drop or a depletion in one of the a-Si:H layers. Charge simulations (shown in Figure S6a and S6b of the Supporting Information) indicate that the large distribution of V_{OC}^{CP} around the well-known macroscopic thermodynamic expectation value $\overline{V_{OC}^{CP}}$ is neither related to the tunneling resistance nor to surface depletion. We therefore hypothesize that it is instead due to local nanoscopic potential fluctuations caused by randomly trapped charges. This hypothesis is quantitatively self-consistent as shown by a simulation of local potential fluctuations caused by the Coulomb fields of randomly spread positive and negative point charges which lead to a random distribution of V_{OC}^{loc} which is expected to show a small TSD dependence as observed experimentally. This result is also consistent with the spread of V_{OC}^{CP} observed in Figure 2d (see also Figure S7 and S8 in the Supporting Information). Previous reports have suggested that above bandgap V_{OC} can exist on the nanometer level if large electric fields (>10 kV/cm) are present as has been observed in ferroelectric photovoltaic devices.[4] With trapped charge in the vicinity of a tail state, electric fields exceeding 500 kV/cm can exist—as compared to the field in the space charge region of the SHJ device being about only 7 kV/cm.

Random Telegraph Noise (RTN)

In order to scrutinize the trapped charge hypothesis described above, we have studied the dynamics of trapping and emission processes in order to see whether this causes dynamical changes to large potential fluctuations resulting in time dependent distributions of I-V curves and hence of V_{OC}. Trapping times of free charge carriers in shallow bandtail or defect states occur on

femtosecond to nanosecond time scales, too fast for the time resolution of our experimental setup.[44-46] However, charge reemission to the bands typically take place on millisecond to second regimes at room temperature for trap depths between 0.7 and 0.8 eV.[22,42] Thus, trapping and emission processes in close proximity of a CP will alter V_{OC}^{loc} locally and should be detectable in the time dependence of the current measured on a CP.

We have measured the transient CuI at various positions of the sample (both, at CPs and within HAs) as indicated in Figure 2e, which displays a CuI as a function of time obtained at an arbitrarily chosen CP. During the measurement, a constant TSD was maintained, using the force-feedback mode of the AFM. The transient CuI clearly exhibits two discrete current levels between which the current fluctuates. The inset in Figure 2e depicts the histogram of the measured current trace, which clearly shows a bimodal distribution. This confirms that the current transient shown in Figure 2e displays random telegraph noise (RTN) as known from electronic processes which are controlled by randomly charged and discharged electronic states.[47]

We have repeatedly measured time-dependent currents on CPs and found RTN in about 25% of the attempts that we have undertaken. No RTN was detected in the HAs. We have then further scrutinized the nature of this effect by verification that the observation of RTN as shown in Figure 2e originates from trapping and reemission of individual electrons in localized electronic states, and not from artifacts, e.g. the presence of impurity molecules (contaminants) on the probe tip or on the surface, as known from previous scanning probe experiments.[48,49] For a detailed experimental analysis we refer to Figure S9 of the Supporting Information. From these experiments, we conclude that the observed RTN must be caused by a mechanism that is inherent to the position where the RTN is detected, i.e. due to an electronic trap and, thus, we conclude that the sample current at some CPs is switched between two levels by local charge trapping and

reemission. Thus, changes of the local potential due to trapping or reemission of charges can dramatically switch the injection properties around the CPs on and off as it has been reported before for doped a-Si:H macroscopic samples.[22-25] Teuschler *et al.* determined that the activation energy of charge capture and emission from deep defects in p-type a-Si:H devices was 0.72 eV and 0.87 eV, respectively, for average switching times of a few 100 ms to a few seconds at RT, comparable to what we observe here.[22] Since in our device only about 25% of the CPs show RTN, we can estimate, following the argumentation of Teuschler *et al.*, that the defect density in our doped a-Si:H layer is about one order of magnitude below the density of bandtail states at the given E_{fp}, which means $N_{\mathrm{db}} \approx 10^{18}$ cm^{-3}, well in accordance with reported estimates the p-type a-Si:H doping levels used here.[42]

CONCLUSION

In summary, using cAFM experiments on the hole selective a-Si:H contact of state-of-the-art SHJ solar cells at RT, we were capable to identify nanoscopic electronic processes which govern the device behaviors. Dark current is governed by trap assisted tunneling through localized states of the valence bandtail states while PC occurs homogeneous across the SHJ area. The tail states are suggested to originate from dense ordered domains that have been reported in a-Si:H which can cluster into larger regions of up to 10 nm well in accordance with our experimental findings.[26] The nanoscopic localization of the bandtail states of the valence band are around found to be about 1 nm well in agreement with what has been estimated from theoretical simulations.[26]

The nanoscopic I-V characteristics of SHJ devices is strongly influenced by fluctuating potentials caused by trapped and detrapping of localized charges at defects in the doped a-Si:H layer, producing local potential fluctuations and, thus, local V_{OC} above 0.8 V, in some few cases even higher than the bandgap. This observation does not violate the fundamental device paradigms

of SHJ solar cells as neither the bandgap nor the local Fermi level is well defined on the nm level. With a current collecting TCO layer, the observed nanoscopic effects will average out, leading to a V_{OC} of 748 mV, in accordance with experiment and macroscopic device simulations.

We also find that the SHJ solar cell at RT provides different nanoscopic pathways for dark current and PC as illustrated by the sketches in Figure 3a-c, which are band diagrams of the SHJ, showing the percolation of PC (Figure 3a) as well as dark current (Figure 3b,c). Note that these band diagrams represent electron energies and localization in a single particle picture, except for the localized electronic bandgap states at the interfaces and within the a-Si:H which are represented in a two-particle picture to avoid ambiguity (see the caption of Figure 3).

Our experiments show that the nanoscopic PC can penetrate the surface at any location, independently of whether a-Si:H bandtail states are present (Figure 3a). In contrast, nanometer-sized CPs emerge under illumination that result from trap-assisted hole injection from the Pt tip through valence bandtail states of the a-Si:H layer into the c-Si where they recombine with electrons injected from the c-Si back contact (Figure 3b). Because of this, the dark current preferentially penetrates the a-Si:H layer stack only at surface locations where bandtail states are present, implying that the performance limiting component of the dark current originates from trap-assisted tunneling in the doped a-Si:H emitter layer of the SHJ device. This effect is observed even for moderate $V_{bias} < V_{OC}$. In order to minimize these tunneling losses, one would need a hole selective a-Si:H layer that does not have bandtail states within reach of the Fermi level of the contact material, since no bandtail states in the energy window of trap assisted tunneling are present at low V_{bias}. For device simulation, the effect of local shunting due to tunneling through bandtail states has to be implemented with a physical model of trap-assisted tunneling. The fact that hole trapping at a defect state in close proximity to the bandtail state (Figure 3c) is occurring

will lead to a shift of the bandtail state to lower energy thereby charging the tail state negatively. The fact that no energetically resonant free states in the Pt tip are available for extracting the electron (or pushing in a hole from the tip) leads to a complete blockade of the injection. If the hole is emitted again from the defect this will lift the injection blockage leading to a strongly (order of 100%) modulated RTN, in good accordance with our observation.

MATERIALS AND METHODS

Sample preparation: The SHJ samples investigated were prepared at Helmholtz-Zentrum Berlin (HZB) and their structure is shown in Figure 1a. The c-Si wafers used are both, n-type and p-type, both sides polished Si <100> oriented 4" quarter wafers. After the RCA cleaning, a three-minute chemical etching process in 1% diluted hydrofluoric (HF) acid on both sides of the c-Si wafers was performed, followed by drying with N_2 gas. The wafers were immediately loaded in the deposition chamber of a two-chamber plasma-enhanced chemical vapor deposition (PECVD) system as illustrated schematically in Scheme 1 to grow the i-a-Si:H (3 nm) and p-a-Si:H (5 nm) layer. Diborane (B_2H_6) was used for p-type doping. Similarly, i-a-Si:H and n-a-Si:H layers were deposited on the back side using PH_3 as doping source. The gas flow ratio of B_2H_6:SiH_4 was 1:27.5. ZnO:Al was deposited as a back-contact electrode using an in-line DC magnetron sputtering system from Leybold Optics (A600V7). Similar fabrication processes were followed to fabricate (n)a-Si:H/(i)a-Si:H/(p)c-Si/(i)a-Si:H/(p)a-Si:H SHJ. More details on the SHJ device fabrication processes can be found elsewhere.[50-54] The SHJ samples were diced (12 mm × 2.85 mm) and clamped onto an Omicron direct-heating molybdenum sample plate holder for cAFM measurements. The native oxide on the front sides of both SHJ samples was removed by a 1% diluted HF etch followed by N_2 drying. The samples were then transferred into the load lock of

Omicron nanotechnology LT-STM UHV system with low-frequency, q-plus quartz tuning fork, within less than five minutes under UHV of 10^{-10} mbar.

Probe preparation: The conductive Pt tips (25Pt300B) were provided by Rocky Mountain Nanotechnology, LCC and were fabricated from solid platinum wires with a tip radius of 20 nm.[38] The tips were bonded by conductive epoxy to the free tune of tuning fork of the qPlus sensor. The sensor with Pt tip was installed in the UHV LT-STM system (Omicron nanotechnology). Tip stability and conductivity were checked by performing STM measurements on 7×7 reconstructed Si (111) surface which was prepared by a standard flash-annealing procedure.[28,29,55] Stable and reproducible atomistically resolved STM images were obtained which verifies the tip stability and conductivity. Once the tip stability and conductivity are verified in this process, cAFM measurements were taken on SHJ samples.

cAFM measurements: The free tune of the qPlus sensor oscillates with a nominal resonance frequency of $f_0 \approx 30$ kHz at a constant amplitude of approximately 1 nm. When a constant forward bias voltage is applied and the tip is within tunneling range, topographic and current images can be simultaneously measured. The frequency shift (Δf) due to tip-sample interaction was kept constant using a height feedback loop. While scanning across the surface, charge-carrier percolation paths with a high lateral resolution in the sub-nanometer range can be detected. Additionally, a single point spectroscopy of I-V characteristics was feasible. The intensity of the white light illumination was performed with a tungsten halogen lamp that was focused through the window access of the cAFM setup. The light intensity of 475 W/m^2 was estimated through comparison with a reference solar cell at the sample position in the cAFM that was calibrated in in a solar simulator (PV measurements QEXL).

ASSOCIATED CONTENT

Supporting Information.

The following files are available free of charge.

Further details related to the distribution of nano-sized local current maxima, the current variation on nanometer-scale, the verification of the constant offset of current detector on the gap and applied bias, the determination of the density of state, the numerical simulations of the structure, the dependence of the open-circuit voltage on the gap size, the simulation of local potential fluctuations, and the evaluation of artifact signals for RTN measurements (PDF)

AUTHOR INFORMATION

Corresponding Author

* boehme@physics.utah.edu

** lips@helmholtz-berlin.de

REFERENCES

(1)   Richter, A.; Hermle, M.; Glunz, S. W. Reassessment of the limiting efficiency for crystalline silicone solar cells. IEEE J. Photovolt. 2013, 3, 1184-1191.

(2)   George, B. M.; Behrends, J.; Schnegg, A.; Schulze, T. F.; Fehr, M.; Korte, L.; Rech, B.; Lips, K.; Rohrmüller, M.; Rauls, E.; Schmidt, W. G.; Gerstmann, U. Atomic structure of interface states in silicon heterojunction solar cells. Phys. Rev. Lett. 2013, 110, 136803.

(3)   Shockley, W.; Queisser, H. J. Detailed balance limit of efficiency of p-n junction solar cells. J. Appl. Phys. 1961, 32, 510-519.

(4)   Yang, S. Y.; Seidel, J.; Byrnes, S. J.; Shafer, P.; Yang, C.-H.; Rossell, M. D.; Yu, P.; Chu, Y.-H.; Scott, J. F.; Ager, J. W.; Martin, L. W.; Ramesh, R. Above-bandgap voltages from ferroelectric photovoltaic devices. *Nat. Nanotechnol.* **2010**, *5*, 143-147.

(5)   Limpert, S.; Burke, A.; Chen, I.-J.; Anttu, N.; Lehmann, S.; Fahlvik, S.; Bremner, S.; Conibeer, G.; Thelander, C.; Pistol, M.-E. Single-nanowire, low-bandgap hot carrier solar cells with tunable open-circuit voltage. *Nanotechnology* **2017**, *28*, 434001.

(6)   Spanier, J. E.; Fridkin, V. M.; Rappe, A. M.; Akbashev, A. R.; Polemi, A.; Qi, Y.; Gu, Z.; Young, S. M.; Hawley, C. J.; Imbrenda, D.; Xiao, G.; Bennett-Jackson, A. L.; Johnson, C. L. Power conversion efficiency exceeding the Shockley-Queisser limit in a ferroelectric insulator. *Nat. Photonics* **2016**, *10*, 611-616.

(7)   Nechache, R.; Harnagea, C.; Li, S.; Cardenas, L.; W., H.; Chakrabartty, J.; Rosei, F. Bandgap tuning of multiferroic oxide solar cells. *Nat. Photonics* **2015**, *9*, 61-67.

(8)   Yang, B.; Yuan, Y.; Sharma, P.; Poddar, S.; Korlacki, R.; Ducharme, S.; Gruverman, A.; Saraf, R.; Huang, J. Tuning the energy level offset between donor and acceptor with ferroelectric dipole layers for increased efficiency in bilayer organic photovoltaic cells. *Adv. Mater.* **2012**, *24*, 1455-1460.

(9)   Seidel, J.; Fu, D.; Yang, S.-Y.; Alarcón-Lladó, E.; Wu, J.; Ramesh, R.; Ager, J. W. Efficient photovoltaic current generation at ferroelectric domain walls. *Phys. Rev. Lett.* **2011**, *107*, 126805.

(10)   Alexe, M.; Hesse, D. Tip-enhanced photovoltaic effects in bismuth ferrite. *Nat. Commun.* **2011**, *2*, 256.

(11)   Dong, J.; Drabold, D. A. Atomistic structure of band-tail states in amorphous silicon. *Phys. Rev. Lett.* **1998**, *80*, 1928-1931.

(12)   van Sark, W. G. J. H. M., Korte, L., Roca, F., Eds. *Physics and technology of amorphous-crystalline heterostructure silicon solar cells;* Engineering materials; Springer, Berlin, Heidelberg, 2012.

(13)   Stangl, R.; Kriegel, M.; Schmidt, M. AFORS-HET, Version 2.2, a numerical computer program for simulation of heterojunction solar cells and measurements. 2006 IEEE 4th World Conference on Photovoltaic Energy Conference. 2006; pp 1350-1353.

(14)   Tanaka, M.; Taguchi, M.; Matsuyama, T.; Sawada, T.; Tsuda, S.; Nakano, S.; Hanafusa, H.; Kuwano, Y. Development of new a-Si/c-Si heterojunction solar cells: ACJ-HIT (artificially constructed junction-heterojunction with intrinsic thin-layer). *Jpn. J. Appl. Phys.* **1992**, *31*, 3518-3522.

(15) Kleider, J.-P.; Alvarez, J.; Ankudinov, A. V.; Gudovskikh, A. S.; Gushchina, E. V.; Labrune, M.; Maslova, O. A.; Favre, W.; Gueunier-Farret, M.-E.; Roca i Cabarrocas, P.; Terukov, E. I. Characterization of silicon heterojunctions for solar cells. *Nanoscale Res. Lett.* **2011**, *6*, 152.

(16) Wiesendanger, R.; Rosenthaler, L.; Hidber, H. R.; Güntherodt, H.-J.; McKinnon, A. W.; Spear, W. E. Hydrogenated amorphous silicon studied by scanning tunneling microscopy. *J. Appl. Phys.* **1988**, *63*, 4515-4517.

(17) Yoshikawa, K.; Kawasaki, H.; Yoshida, W.; Irie, T.; Konishi, K.; Nakano, K.; Uto, T.; Adachi, D.; Kanematsu, M.; Uzu, H.; Yamamoto, K. Silicon heterojunction solar cell with interdigitated back contacts for a photoconversion efficiency over 26%. *Nat. Energy* **2017**, *2*, 17032.

(18) Masuko, K.; Shigematsu, M.; Hashiguchi, T.; Fujishima, D.; Kai, M.; Yoshimura, N.; Yamaguchi, T.; Ichihashi, Y.; Mishima, T.; Matsubara, N.; Yamanishi, T.; Takahama, T.; Taguchi, M.; Maruyama, E.; Okamoto, S. Achievement of more than 25% conversion efficiency with crystalline silicon heterojunction solar cell. *IEEE J. Photovoltaics* **2014**, *4*, 1433-1435.

(19) Nakamura, J.; Asano, N.; Hieda, T.; Okamoto, C.; Katayama, H.; Nakamura, K. Development of heterojunction back contact Si solar cells. *IEEE J. Photovoltaics* **2014**, *4*, 1491-1495.

(20) Smith, D. D.; Cousins, P.; Westerberg, S.; Jesus-Tabajonda, R. D.; Aniero, G.; Shen, Y.-C. Toward the practical limits of silicon solar cells. *IEEE J. Photovoltaics* **2014**, *4*, 1465-1469.

(21) Yoshikawa, K.; Yoshida, W.; Irie, T.; Kawasaki, H.; Konishi, K.; Ishibashi, H.; Asatani, T.; Adachi, D.; Kanematsu, M.; Uzu, H.; Yamamoto, K. Exceeding conversion efficiency of 26%

by heterojunction interdigitated back contact solar cell with thin film Si technology. *Sol. Energy Mater. Sol. Cells* **2017**, *173*, 37-42.

(22). Teuschler, T.; Hundhausen, M.; Ley, L.; Arce, R. Analysis of random telegraph noise in large-area amorphous double-barrier structures. *Phys. Rev. B* **1993**, *47*, 12687-12695.

(23) Parman, C. E.; Israeloff, N. E.; Kakalios, J. Random telegraph-switching noise in coplanar current measurements of amorphous silicon. *Phys. Rev. B* **1991**, *44*, 8391-8394.

(24) Choi, W. K.; Owen, A. E.; LeComber, P. G.; Rose, M. J. Exploratory observations of random telegraphic signals and noise in homogeneous hydrogenated amorphous silicon. *J. Appl. Phys.* **1990**, *68*, 120-123.

(25) Arce, R.; Ley, L. Observation of random telegraphic noise in large area a-Si:H/a-Si$_{1-x}$N$_x$:H double barrier structures. *MRS Online Proc. Libr.* **1989**, *149* 696-697.

(26) Gericke, E.; Melskens, J.; Wendt, R.; Wollgarten, M.; Hoell, A.; Lips, K. Quantification of nanoscale density fluctuations in hydrogenated amorphous silicon. Phys. Rev. Lett. **2020**, *125,* 185501.

(27) Al-Ashouri, A.; Köhnen, E.; Li, B.; Magomedov, A.; Hempel, H.; Caprioglio, P.; Márquez, J. A.; Morales Vilches, A. B.; Kasparavicius, E.; Smith, J. A.; Phung, N.; Menzel, D.; Grischek, M.; Kegelmann, L; Skroblin, D.; Gollwitzer, C.; Malinauskas, T.; Jošt, M.; Matič, G.; Rech, B.; Schlatmann, R.; Topič, M.; Korte, L.; Abate, A.; Stannowski, B.; Neher, D.; Stolterfoht, M.; Unold, T.; Getautis, V.; Albrecht, S. Monolithic perovskite/silicon tandem solar cell with >29% efficiency by enhanced hole extraction. *Science* **2020**, *370*, 1300-1309.

(28) Giessibl, F. J. The qPlus sensor, a powerful core for the atomic force microscope. *Rev. Sci. Instrum.* **2019**, *90*, 011101.

(29) Ohnesorge, F.; Binnig, G. True Atomic Resolution by Atomic Force Microscopy Through Repulsive and Attractive Forces. *Science* **1993**, *260*, 1451-1456.

(30) Majzik, Z.; Setvín, M.; Bettac, A.; Feltz, A.; Chäb, V.; Jelínek, P. Simultaneous current, force and dissipation measurements on the Si(111) 7×7 surface with an optimized qPlus AFM/STM technique. *Beilstein J. Nanotechnol.* **2012**, *3*, 249-259.

(31) Giessibl, F. J. Atomic Resolution of the Silicon (111)-(7x7) Surface by Atomic Force Microscopy. *Science* **1995**, *267*, 68-71.

(32) MacDonald, G. A.; Yang, M.; Berweger, S.; Killgore, J. P.; Kabos, P.; Berry, J. J.; Zhu, K.; DelRio, F. W. Methylammonium lead iodide grain boundaries exhibit depth-dependent electrical properties. *Energy Environ. Sci.* **2016**, *9*, 3642-3649.

(33) Luria, J.; Kutes, Y.; Moore, A.; Zhang, L.; Stach, E. A.; Huey, B. D. Charge transport in CdTe solar cells revealed by conductive tomographic atomic force microscopy. *Nat. Energy* **2016**, *1*, 16150.

(34) Kutes, Y.; Aguirre, B. A.; Bosse, J. L.; Cruz-Campa, J. L.; Zubia, D.; Huey, B. D. Mapping photovoltaic performance with nanoscale resolution. *Prog. Photovoltaics* **2015**, *24*, 315-325.

(35) Cruz, A.; Wang, E.-C.; Morales-Vilches, A. B.; Meza, D.; Neubert, S.; Szyszka, B.; Schlatmann, R.; Stannowski, B. Effect of front TCO on the performance of rear-junction silicon heterojunction solar cells: Insights from simulations and experiments. *Sol. Energy Mater. Sol. Cells* **2019**, *195*, 339-345.

(36) 35. Wang, E.-C.; Morales-Vilches, A. B.; Neubert, S.; Cruz, A.; Schlatmann, R.; Stannowski, B. A simple method with analytical model to extract heterojunction solar cell series resistance components and to extract the A-Si:H(i/p) to transparent conductive oxide contact resistivity. *AIP Conf. Proc.* **2019**, *2147*, 040022.

(37) Morales-Vilches, A. B.; Cruz, A.; Pingel, S.; Neubert, S.; Mazzarella, L.; Meza, D.; Korte, L.; Schlatmann, R.; Stannowski, B. ITO-Free Silicon Heterojunction Solar Cells With ZnO:Al/SiO$_2$ Front Electrodes Reaching a Conversion Efficiency of 23%. *IEEE J. Photovoltaics* **2019**, *9*, 34-39.

(38) Rocky Mountain Nanotechnology, LLC. https://rmnano.com/probes (accessed Sep 14, 2020).

(39) The CuI is the sum of the dark current and the photocurrent (PC). Due to the superposition principle, the PC in classical p-n junction theory is independent of voltage and is determined by the light-induced generation rate and the internal collection efficiency.

(40) Ambal, K.; Rahe, P.; Payne, A.; Slinkman, J.; Williams, C. C.; Boehme, C. Electrical current through individual pairs of phosphorus donor atoms and silicon dangling bonds. *Sci. Rep.* **2016**, *6*, 18531.

(41) Sentaurus Structure Editor User Guide. Synopsys, Inc., 2011.

(42) Street, R. A. *Hydrogenated Amorphous Silicon*; Cambridge University Press, 1991.

(43) McGlynn, S. P. Concepts in Photoconductivity and Allied Problems. *J. Am. Chem. Soc.* **1964**, *86*, 5707-5707.

(44) Jepsen, P. U.; Schairer, W.; Libon, I. H.; Lemmer, U.; Hecker, N. E.; Birkholz, M.; Lips, K.; Schall, M. Ultrafast carrier trapping in microcrystalline silicon observed in optical pump-terahertz probe measurements. *Appl. Phys. Lett.* **2001**, *79*, 1291-1293.

(45) Nebel, C. E.; Bauer, G. H. Tail-state distribution and trapping probability in a-Si:H investigated by time-of-flight experiments and computer simulations. *Philos. Mag. B* **1989**, *59*, 463-479.

(46) Fekete, L.; Kužel, P.; Němec, H.; Kadlec, F.; Dejneka, A.; Stuchlík, J.; Fejfar, A. Ultrafast carrier dynamics in microcrystalline silicon probed by time-resolved terahertz spectroscopy. *Phys. Rev. B* **2009**, *79*, 115306.

(47) Neri, B.; Olivo, P.; Riccò, B. Low-frequency noise in silicon-gate metal-oxide-silicon capacitors before oxide breakdown. *Appl. Phys. Lett.* **1987**, *51*, 2167-2169.

(48) Chen, F.; Huang, Z.; Tao, N. Forming single molecular junctions between indium tin oxide electrodes. *Appl. Phys. Lett.* **2007**, *91*, 162106.

(49) Xu, B. Measurement of Single-Molecule Resistance by Repeated Formation of Molecular Junctions. *Science* **2003**, *301*, 1221-1223.

(50) Mazzarella, L.; Kirner, S.; Mews, M.; Conrad, E.; Korte, L.; Stannowski, B.; Rech, B.; Schlatmann, R. Comparison of TMB and B_2H_6 as Precursors for Emitter Doping in High Efficiency Silicon Hetero Junction Solar Cells. *Energy Procedia* **2014**, *60*, 123-128.

(51) Mazzarella, L.; Morales-Vilches, A. B.; Hendrichs, M.; Kirner, S.; Korte, L.; Schlatmann, R.; Stannowski, B. Nanocrystalline n-Type Silicon Oxide Front Contacts for Silicon

Heterojunction Solar Cells: Photocurrent Enhancement on Planar and Textured Substrates. *IEEE J. Photovoltaics* **2018**, *8*, 70-78.

(52) Mazzarella, L.; Kirner, S.; Gabriel, O.; Schmidt, S. S.; Korte, L.; Stannowski, B.; Rech, B.; Schlatmann, R. Nanocrystalline silicon emitter optimization for Si-HJ solar cells: Substrate selectivity and CO_2 plasma treatment effect. *Phys. Status Solidi A* **2017**, *214*, 1532958.

(53) Morales-Vilches, A. B.; Wang, E.-C.; Henschel, T.; Kubicki, A. C.; Janke, S.; Korte, L.; Schlatmann, R.; Stannowski, B. Improved Surface Passivation by Wet Texturing, Ozone- Based Cleaning, and Plasma-Enhanced Chemical Vapor Deposition Processes for High-Efficiency Silicon Heterojunction Solar Cells. *Phys. Status Solidi A* **2019**, *217*, 1900518.

(54) Gabriel, O.; Kirner, S.; Klick, M.; Stannowski, B.; Schlatmann, R. Plasma monitoring and PECVD process control in thin film silicon-based solar cell manufacturing. *EPJ Photovolt.* **2014**, *5*, 55202.

(55) Chen, C. *Introduction to scanning tunneling microscopy*; Oxford University Press: Oxford New York, 2008.

Graphical TOC Entry